

# Measurement of the $(\gamma, n)$ reaction rates of the nuclides $^{190}\text{Pt}$ , $^{192}\text{Pt}$ , and $^{198}\text{Pt}$ in the astrophysical $\gamma$ process

K. Vogt,<sup>1</sup> P. Mohr,<sup>1</sup> M. Babilon,<sup>1</sup> J. Enders,<sup>1</sup> T. Hartmann,<sup>1</sup> C. Hutter,<sup>1</sup> T. Rauscher,<sup>2,3</sup> S. Volz,<sup>1</sup> A. Zilges<sup>1</sup>

<sup>1</sup> *Institut für Kernphysik, Technische Universität Darmstadt, Schlossgartenstrasse 9, D-64289 Darmstadt, Germany*

<sup>2</sup> *Institut für Physik, Universität Basel, Klingelbergstrasse 82, CH-4056 Basel, Switzerland*

<sup>3</sup> *Department of Astronomy and Astrophysics, UCSC, Santa Cruz, CA 95064, USA*

(October 26, 2018)

The nucleosynthesis of heavy neutron-deficient nuclei in a stellar photon bath at the temperatures relevant for the astrophysical  $\gamma$  process was investigated. In order to derive  $(\gamma, n)$  cross sections and reaction rates, the stellar photon bath was simulated by the superposition of several bremsstrahlung spectra with different endpoint energies. As a first test for this method, the  $(\gamma, n)$  reaction rates of the platinum isotopes  $^{190}\text{Pt}$ ,  $^{192}\text{Pt}$ , and  $^{198}\text{Pt}$  were derived. The results are compared to other experimental data and theoretical calculations.

PACS numbers: 25.20.-x, 26.30.+k, 98.80.Ft, 26.45.+h

## I. INTRODUCTION

The bulk of the nuclei heavier than iron have been synthesized by neutron capture in the astrophysical  $r$  and  $s$  processes. Those neutron-capture processes cannot account for the synthesis of some of the heavy ( $A \geq 100$ ) neutron-deficient nuclei. These nuclei are shielded from the chain of  $\beta^-$  decays by other stable isobars. The production mechanism for these so-called p-nuclei is photo-disintegration in the astrophysical  $\gamma$  process by successive  $(\gamma, n)$ ,  $(\gamma, p)$ , and  $(\gamma, \alpha)$  reactions. The natural abundances for the p-nuclei are very low in the order of 0.01 % to 1 %. A complete list of the p-nuclei can be found in Table 1 of Ref. [1]. The starting point for the photon-induced reactions are heavy seed nuclei which have been synthesized in the  $r$  and  $s$  processes.

In order to reproduce the abundances of p-nuclei measured in the solar system, temperatures in the  $\gamma$  process must be in the range of  $T_9 = 2 - 3$  ( $T_9$  is the temperature in  $10^9$  K), densities about  $\rho \approx 10^6$  g/cm<sup>3</sup>, and time scales  $\tau$  of the order of seconds. A possible astrophysical site which fulfills these requirements could be the oxygen- and neon-rich layers of type II supernovae. However, there has been no definite conclusion to this question yet. Details about the  $\gamma$  process and its astrophysical scenarios can be found in the reviews by Lambert [1], Arnould and Takahashi [2], Langanke [3], Wallerstein *et al.* [4] and in Refs. [5–10].

For the calculation of the p-nuclei abundances resulting from the  $\gamma$  process, large reaction networks containing all relevant nuclei and reaction rates are needed [7]. Until now, there have been almost no experimental data available for these reaction rates in the relevant energy region. Although in the last decades a large number of  $(\gamma, n)$  cross sections have been measured around the giant dipole resonance (GDR), the energies of astrophysical interest are much lower, and practically no data exist for the p-nuclei because of their low abundance. All reaction rates have

been derived theoretically, using statistical model calculations. Reliable experimental data would be a great improvement to reduce the nuclear physics uncertainties of astrophysical model calculations, especially because of the typical uncertainties of such statistical model calculations which are at least of the order of a factor of 2.

As a starting point for the measurement of the needed reaction rates, we have measured the  $(\gamma, n)$  reaction rates of the platinum isotopes  $^{190}\text{Pt}$  (natural abundance: 0.014%),  $^{192}\text{Pt}$  (0.782%), and  $^{198}\text{Pt}$  (7.163%). The natural abundances have been taken from [11]. The  $(\gamma, n)$  reaction rate for a nucleus in a thermal photon bath is given by

$$\lambda(T) = \int_0^\infty c n_\gamma(E, T) \sigma_{(\gamma, n)}(E) dE \quad (1.1)$$

with the speed of light  $c$  and the cross section of the  $(\gamma, n)$  reaction  $\sigma_{(\gamma, n)}$ . The number of photons  $n_\gamma(E, T)$  at energy  $E$  per unit of volume and per energy interval is given by the well-known Planck distribution

$$n_\gamma(E, T) = \left(\frac{1}{\pi}\right)^2 \left(\frac{1}{\hbar c}\right)^3 \frac{E^2}{\exp(E/kT) - 1} \quad (1.2)$$

For the measurement of the  $(\gamma, n)$  reaction rates we used the method of photoactivation. We irradiated platinum samples with bremsstrahlung. Then we measured the number of decays of generated unstable platinum nuclei  $^{189,191,197}\text{Pt}$ .

The biggest difficulty in the determination of the  $(\gamma, n)$  reaction rates is the reproduction of the thermal photon bath. In our experiment, the platinum samples were irradiated with bremsstrahlung. We are able to generate a quasi-thermal photon spectrum in the relevant energy region by the superposition of several bremsstrahlung spectra with different endpoint energies. This idea has been presented in our previous paper [12].

## II. EXPERIMENTAL SETUP

The irradiation of the platinum samples was performed at the real photon facility of the superconducting Darmstadt linear electron accelerator S-DALINAC [13–15]. This setup is mainly used for Nuclear Resonance Fluorescence experiments which can be performed up to endpoint energies of 10 MeV without disturbing neutron-induced background [14].

As targets we used metallic platinum disks of natural isotopic composition with a diameter of  $2r = 20$  mm and a thickness of  $d = 0.125$  mm with masses of around 800 mg. The platinum disks were sandwiched between two thin boron layers with masses of about 650 mg each. In order to normalize the photon flux we measured spectra of resonantly scattered photons from nuclear levels of  $^{11}\text{B}$  during the activation. For this measurement, we used two high purity germanium (HPGe) detectors with 100 % efficiency (relative to a  $3'' \times 3''$  NaI detector) which were mounted at  $90^\circ$  and  $127^\circ$  relative to the beam axis of the incoming photons. Further information on the  $(\gamma, \gamma')$  experiments can be found in [16].

The platinum samples were irradiated for about 24 h, then their activity was measured for another 24 h. For the measurement of the activity the samples were mounted directly in front of a third HPGe detector with 30 % relative efficiency. Some typical activation spectra are shown in Fig. 1. Altogether, six measurements with endpoint energies of the bremsstrahlung spectra between 7650 – 9900 keV in steps of 450 keV were performed.

## III. ANALYSIS OF THE EXPERIMENTAL DATA

The aim of this experiment was the determination of the  $(\gamma, n)$  reaction rates of several platinum isotopes. These reaction rates are given by Eq. (1.1).

The result of the analysis of the platinum activation spectra is an integral over the  $(\gamma, n)$  cross section:

$$I_\sigma = \int_0^\infty N_\gamma^{\text{brems}}(E_0, E) \sigma_{(\gamma, n)}(E) dE \quad (3.1)$$

where  $N_\gamma^{\text{brems}}(E_0, E)$  is the total number of bremsstrahlung photons at energy  $E$  per area and per energy interval during the irradiation.  $E_0$  is the endpoint energy of the respective bremsstrahlung spectrum. In order to determine the  $(\gamma, n)$  reaction rates from these results we used two different methods (see Sect. III B, III C).

### A. The Gamow-like window for $(\gamma, n)$ reactions

The integrand of Eq. (1.1) is given by the product of the photon flux  $cn_\gamma$ , which decreases exponentially

with increasing energy, and the  $(\gamma, n)$  cross section  $\sigma_{(\gamma, n)}$ , which increases with  $E$  to the Giant Dipole Resonance (GDR). Additionally, the threshold behavior has to be parametrized because the Lorentzian parametrization of the GDR is not valid close to the  $(\gamma, n)$  threshold (see Sect. III B). The Planck distribution, a typical  $(\gamma, n)$  cross section, and the resulting integrand of Eq. (1.1) are shown in Fig. 2 for  $^{198}\text{Pt}$  at  $T_9 = 3.0$ . The maximum of the integrand is located at about  $kT/2$  above the  $(\gamma, n)$  threshold. The behavior of the integrand is similar to the well-known Gamow window (see e.g. Ref. [17]) for charged particle reactions at thermonuclear energies. The properties of the window for  $(\gamma, n)$  reactions have been discussed in detail in [18].

### B. The conventional analysis

One can assume the shape of the  $(\gamma, n)$  cross section to show a typical threshold behavior:

$$\sigma(E) = \sigma_0 \cdot \sqrt{(E - E_{\text{thr}})/E_{\text{thr}}} \quad (3.2)$$

This equation holds only in the vicinity of the reaction threshold. Nevertheless, it should be sufficiently accurate since only a small energy region above the threshold energy is relevant for the analysis. By combining Eqs. (3.1) and (3.2) it is possible to derive the parameter  $\sigma_0$  from our experimental data. From the parameter  $\sigma_0$  we calculated the  $(\gamma, n)$  reaction rate using Eq. (1.1). The serious drawback of this method is that it is not possible to estimate how much the real shape of  $\sigma(E)$  deviates from the approximation by Eq. (3.2).

### C. The superposition of bremsstrahlung spectra

In order to derive the  $(\gamma, n)$  reaction rates directly from our experimental data, that is to say without any assumptions on the shape of the  $\sigma(E)$  curve, we approximated the thermal Planck spectrum  $n_\gamma(E, T)$  in Eq. (1.2) by the superposition of several bremsstrahlung spectra with different endpoint energies:

$$cn_\gamma(E, T) \approx \sum_i a_i(T) \cdot N_\gamma^{\text{brems}}(E_{0,i}, E) \quad (3.3)$$

where the  $a_i(T)$  are strength coefficients which have to be adjusted for each temperature  $T$ . With these strength coefficients, the  $(\gamma, n)$  reaction rates can be obtained by combining Eq. (3.3) with Eq. (1.1):

$$\lambda(T) = \sum_{i=1}^N a_i(T) \cdot \int N_\gamma^{\text{brems}}(E_{0,i}, E) \sigma(E) dE \quad (3.4)$$

An example for this superposition is shown in Fig. 3. In the energy range from 7.5 to 10 MeV the agreement

between the thermal Planck spectrum at  $T_9 = 2.0$  and the weighted sum of the different bremsstrahlung spectra is reasonably good. Typical deviations are of the order of 10%. Obviously, the huge deviations at energies below the  $(\gamma, n)$  reaction threshold are not relevant for our analysis.

#### D. Analysis of the platinum activation spectra

Fig. 1 shows three partial platinum activation spectra. Lines from the decay of the platinum isotopes  $^{189}\text{Pt}$ ,  $^{191}\text{Pt}$ , and  $^{197}\text{Pt}$  can clearly be identified in the upper spectrum which shows the decay of a platinum sample which has been irradiated with a bremsstrahlung spectrum with an endpoint energy of 9900 keV. In the two lower spectra, which correspond to endpoint energies of 9450 keV and 9000 keV, respectively, the lines from the decay of  $^{189}\text{Pt}$  and  $^{191}\text{Pt}$  vanish because the endpoint energies of the bremsstrahlung get close to the neutron separation energies of these isotopes (see Table I). In the complete activation spectrum (see [12]) several additional lines, including two lines from the decay of  $^{195m}\text{Pt}$  can be identified; this isomer is mainly populated by the  $(\gamma, \gamma')$  reaction. The spectra were analyzed using the computer code tv [19].

For the derivation of the  $(\gamma, n)$  reaction rates of the platinum isotopes  $^{190}\text{Pt}$ ,  $^{192}\text{Pt}$  and  $^{198}\text{Pt}$ , the integral (3.1) must be calculated from the number of counts  $A$  in the decay lines of the platinum isotopes  $^{189}\text{Pt}$ ,  $^{191}\text{Pt}$  and  $^{197}\text{Pt}$ , respectively. The dependence of these quantities is given by

$$A = \epsilon \cdot I_\gamma \cdot \frac{T_{\text{life}}}{T_{\text{real}}} \cdot \frac{N_{\text{decay}}}{N_{\text{total}}} \cdot N_{\text{Pt}} \cdot \int \sigma(E) N_\gamma^{\text{brems}} dE \quad (3.5)$$

where  $\epsilon$  is the absolute detector efficiency,  $I_\gamma$  the absolute intensity of the platinum decay lines per decay,  $T_{\text{life}}/T_{\text{real}}$  the ratio from lifetime to realtime, and  $N_{\text{Pt}}$  the total number of platinum nuclei of the respective isotope in the target.  $N_{\text{decay}}/N_{\text{total}}$  is the ratio between the number of nuclei which decay during the measurement and the total number of produced unstable nuclei. This ratio is given by:

$$N_{\text{decay}}/N_{\text{total}} = e^{-\lambda T_{\text{loss}}} \cdot \frac{(1 - e^{-\lambda T_{\text{irr}}})}{\lambda T_{\text{irr}}} \cdot (1 - e^{-\lambda T_{\text{measure}}}) \quad (3.6)$$

where  $T_{\text{measure}}$  is the duration of the measurement,  $T_{\text{irr}}$  the duration of the irradiation, and  $T_{\text{loss}}$  the time between the end of the irradiation and the beginning of the measurement. These equations only hold for a constant production rate during the irradiation, which is approximately given for our experiment since the electron beam current was approximately constant.

The energies and relative intensities of the examined lines of the platinum isotopes are shown in Table I. Note that the relatively big uncertainties in the absolute intensities are responsible for the major part of the errors in our results as seen in Table II.

For the calculation of the factor  $N_{\text{decay}}/N_{\text{total}}$ , precise knowledge of the half-lives of the produced unstable platinum isotopes is necessary. Because of that, those half-lives have been determined in an additional measurement [20].

#### E. Determination of the photon flux

For the approximation of the thermal Planck spectrum the precise shape of the different bremsstrahlung spectra especially in the high energy region had to be determined. Therefore Monte Carlo simulations using the computer code GEANT [21] were performed. To check the uncertainties of the GEANT calculations  $(\gamma, \gamma')$  measurements of well known  $^{11}\text{B}$  lines have been performed during the irradiation of the platinum samples in order to normalize the GEANT generated photon spectra. At the energies of these  $^{11}\text{B}$  lines, the absolute photon flux could be calculated. For these calculations, the efficiencies of the two detectors used for the measurement during the irradiation of the platinum samples had to be calibrated up to the energy of 10 MeV (see Sect. III F).

However, the shape of the bremsstrahlung spectra derived from the results of the  $(\gamma, \gamma')$  measurements and the spectra from the GEANT calculations show deviations near the endpoint energy. Unfortunately, the shape of the bremsstrahlung spectra could not be determined by the  $^{11}\text{B}$  lines alone, because there are only two lines (see Tab. III) in the high energy region.

Therefore, we tried to reproduce the measured  $^{11}\text{B}$  lines by using theoretical formulas. The energy distribution of bremsstrahlung is approximately given by the Schiff formula [23]. However, this formula is only valid for bremsstrahlung from thin radiator targets, which means that each electron participates only in one scattering process and therefore emits only one photon. In our experiment, the electron beam was completely stopped within the radiator target. Thus, neither the Schiff formula nor newer approximation formulas given by Seltzer and Berger [24] reproduce the shape of our bremsstrahlung spectra with sufficient accuracy. Especially in the high energy region, the deviations are still considerable.

Therefore, the shape of the bremsstrahlung spectra was interpolated in the high energy region between 80 % and 100 % of the endpoint energy using cubic splines with the  $^{11}\text{B}$  lines as points of support. Unfortunately, in the spectrum with the lowest endpoint energy of 7650 keV, no  $^{11}\text{B}$  line can be seen in the relevant energy region. Therefore, no points of support are available for

the spline interpolation of this spectrum. So we adjusted the GEANT calculated spectra in the high energy region by multiplying an energy-dependent correction factor  $F$ :

$$F = \begin{cases} 1 - 5 \cdot 10^{-4} \cdot \left(\frac{E - 0.8E_0}{\text{keV}}\right)^{3/4} & ; E > 0.8 E_0 \\ 1 & ; E \leq 0.8 E_0 \end{cases} \quad (3.7)$$

where  $E_0$  is the endpoint energy of the respective bremsstrahlung spectra. The shapes of the bremsstrahlung spectra resulting from both methods are shown in Fig. 4 for all measured endpoint energies. The results of the spline interpolation are represented by the dashed lines, the results of the GEANT simulations multiplied by the correction factor  $F$  are represented by the straight lines. The good overall agreement between these curves and the data points of the  $^{11}\text{B}$  measurements is quite satisfactory. Since the spline interpolation is not reliable for the spectrum with 7650 keV endpoint energy, we used the bremsstrahlung spectra adjusted by the correction factor  $F$  for the calculations of the reaction rates. The correction factor  $F$  leads to a significant reduction of the photon flux close to the endpoint energy  $E_0$ . A precise knowledge of this energy region is essential for the superposition of the quasi-thermal spectrum. If one neglects this correction in the bremsstrahlung spectra, the reaction rates are underestimated by up to a factor of 2.

## F. Determination of detector efficiencies

### 1. Detectors for photon flux normalization

The calibration measurement was performed in two steps. First, a measurement of the absolute efficiency using  $^{60}\text{Co}$ ,  $^{137}\text{Cs}$ , and  $^{22}\text{Na}$  calibration sources was performed. This was followed by a second measurement using a  $^{56}\text{Co}$  source. Since the intensity of this source was not calibrated, only a relative efficiency could be determined, but these data points were adjusted to fit those of the absolute efficiency measurement. Since there were no decay lines of these sources at energies above 3548.3 keV, an additional GEANT calculation was performed to determine the efficiency in the high energy region.

As can be seen in Fig. 5, the results of the measurement and the calculation correspond well with each other, and it has been shown that the detection efficiencies of large volume HPGe detectors can be calculated with good accuracy [22]. The decrease in the efficiency at low energies results from lead and copper filters which were mounted in front of the detectors in order to reduce low energy background.

### 2. Detector for activation measurements

Because the activity of the platinum samples was relatively low, they have been mounted directly in front of the 30 % HPGe detector used for the activation measurement. Since the activity of the available calibration sources was much higher, only a small number of lines could be used for the calibration measurements of the HPGe detector. However, some of the calculated data points for the efficiency still have relatively big errors, as is shown in Fig. 6. These errors are mainly due to summing effects resulting from the high count rate of the detector. For the calculations we used a doubly logarithmic interpolation of the data points in the relevant energy interval.

It had to be considered that due to the thickness of the platinum disks of 0.125 mm a portion of the emitted  $\gamma$  rays was absorbed within the disks. This portion has been estimated using the computer code GEANT. The necessary corrections were of the order of a few percent, except for the 77.4 keV line of the  $^{197}\text{Pt}$ , where approximately two thirds of the  $\gamma$  rays were absorbed within the platinum sample.

## IV. EXPERIMENTAL RESULTS

### A. Results for the cross section $\sigma_{(\gamma,n)}$

The cross section parameters  $\sigma_0$  from Eq. (3.2) have been calculated twice for every isotope, using both the spline interpolated and the by the factor  $F$  corrected photon spectra. The two results are given in Tab. II, averaged over all measurements with different endpoint energies.

For  $^{190}\text{Pt}$  an additional measurement has been performed. This was necessary because the evaluation of the  $^{190}\text{Pt}$  lines was close to the statistical limit. For this measurement the platinum target was placed directly behind the radiator target because of the much higher photon flux. In this target position the  $(\gamma, \gamma')$  lines of the  $^{11}\text{B}$  samples could not be measured. Therefore, the shape of the photon spectrum could not be determined. However, since the neutron separation energies of  $^{190}\text{Pt}$  and of  $^{192}\text{Pt}$  are close to each other (Tab. II), we were able to calculate the ratio of the cross sections of these isotopes by determining the ratio of the number of counts in their respective lines. Then we calculated the cross section of  $^{190}\text{Pt}$  by multiplying this ratio with the known value for the cross section of  $^{192}\text{Pt}$  from the previous measurement. This value is considered in the average in Tab. II.

For the calculation of errors, the uncertainties in the detector efficiencies, the statistical errors from the number of counts in the respective peaks and the errors in the relative and absolute intensities of the decay lines

have been considered. In order to estimate the error resulting from the uncertainty in the shape of the photon spectra, we calculated the mean difference of the interpolated spectra and the spectra which were adjusted by the correction factor  $F$ . For  $^{190}\text{Pt}$  an additional error of 7% has been considered, resulting from an uncertainty in the natural abundance of this isotope.

### B. Results for the $(\gamma, n)$ reaction rates

The  $(\gamma, n)$  reaction rates  $\lambda$  have been determined from  $\sigma_0$  and with the superposition method (see Sect. III). With both methods, the reaction rates in the complete relevant temperature region ( $T_9 = 2 - 3$ ) have been calculated. The results are given in Tables IV, V, and VI. These results are averaged over all evaluated lines of the respective isotopes. For the superposition of the bremsstrahlung spectra, the bremsstrahlung spectra adjusted by the correction factor  $F$  of Eq. (3.7) have been used. For the conventional method, only the values of  $\sigma_0$  calculated with the corrected photon spectra have been used in order to be able to compare the results of both methods. For the isotope  $^{190}\text{Pt}$  the superposition method could not be used because the decay lines of  $^{189}\text{Pt}$  could not be evaluated in all measurements. For this isotope the average value of  $\sigma_0$  which is given in Tab. II has been used for the calculation in the conventional method. The relative errors for the reaction rates calculated by the conventional method are the same as the error for the parameter  $\sigma_0$ .

The temperature dependence of the reaction rates is shown in Fig. 7 for the isotopes  $^{190}\text{Pt}$ ,  $^{192}\text{Pt}$ , and  $^{198}\text{Pt}$ . The given values are calculated using the superposition method. The comparison of the results of both methods shows good overall agreement. The error of the conventional method seems to be smaller than the error of the superposition method because of the additional error resulting from the difference between thermal and superposed photon spectra. It has to be pointed out that the most important systematic uncertainty in the conventional method cannot be estimated, i.e. the uncertainty how good Eq. (3.2) approximates the shape of the cross section energy dependence. Therefore, the superposition method should prove much more reliable.

### C. Comparison with other results

In Fig. 8 our result for the  $(\gamma, n)$  cross section of the isotope  $^{198}\text{Pt}$  is compared with a previous experiment by Goryachev *et al.* [25]. They measured the  $(\gamma, n)$  cross section at various energies in and below the GDR region whereas we determined the cross section parameter  $\sigma_0$ . Therefore a comparison of both results is only possible if one assumes the behavior of the cross section to follow

Eq. (3.2). Since this parametrization only holds in the vicinity of the threshold energy, the deviations at higher energies are not surprising.

Previous direct experiments had to be performed with huge amounts of highly enriched target material of the order of several grams. Such an amount of highly enriched material is not available for the low abundant platinum isotopes  $^{190}\text{Pt}$  and  $^{192}\text{Pt}$ , and hence no data exist in literature for these isotopes and for the p isotopes of other elements [26,27]. To our knowledge our data are the first experimental  $(\gamma, n)$  cross sections and astrophysical reaction rates measured for the p-nuclei.

## V. THEORETICAL CONSIDERATIONS

### A. Calculation of laboratory and stellar rates

Experimental data can only provide photodisintegration rates of targets in their ground state. In a stellar plasma of the required temperature and density, nuclei are thermally equilibrated with their environment and therefore also excited states will be populated. The laboratory cross section  $\sigma_{(\gamma, n)}^{\text{lab}} = \sum_{\nu} \sigma^{0\nu}$  has to be replaced by the stellar cross section

$$\sigma^*(E, T) = \frac{\sum_{\mu} (2J^{\mu} + 1) \exp(-E^{\mu}/kT) \sum_{\nu} \sigma^{\mu\nu}(E)}{\sum_{\mu} (2J^{\mu} + 1) \exp(-E^{\mu}/kT)}, \quad (5.1)$$

where  $\mu$  and  $\nu$  denote the target states and the states in the final nucleus, respectively. Depending on plasma temperature  $T$ , spins  $J^{\mu}$  and location  $E^{\mu}$  of the target states, the stellar cross section can become considerably different from the one measured in the laboratory.

Up to now, astrophysical photodisintegration rates were calculated in a purely theoretical way by deriving them from capture rates via detailed balance (e.g. [31–33]). It should be noted that only *stellar* capture rates can be used to correctly apply detailed balance and, vice versa, only stellar photodisintegration rates can be used for the derivation of the respective stellar capture rates. Those stellar capture rates are usually also calculated theoretically. Detailed balance is valid for exoergic reactions ( $Q > 0$ ) and it has recently been shown that it is still quite accurate for charged particle capture with  $Q < 0$  [34].

Nevertheless, laboratory measurements are an important way to check the validity of the involved assumptions and the nuclear properties needed for the prediction of cross sections and rates. A direct measurement of the  $(\gamma, n)$  cross section can not only test detailed balance but also the description used for the low-energy tail of the GDR and the neutron optical potential for nuclei in excited states. Measurements using neutron capture are more limited in this respect.

Here, we compare the experimental results to calculations with the statistical model code NON-SMOKER [33]. For the calculations presented here, the code NON-SMOKER was modified in such a way to be able to calculate photodisintegration reactions directly instead of deriving them via detailed balance (like e.g. in Ref. [33]). This modification also allows to compute rates for targets in the ground state which can easily be compared to our experimental results. The theoretical results are collected in Tab. VII and a comparison to the data is shown in Tab. VIII.

## B. Discussion

In general, the theoretical rates are in good agreement with the present data, as can be seen from Tab. VIII. For the global statistical model calculations compared here, a typical average deviation of the order of 30 % should be expected but locally larger deviations up to a factor of two are possible. In this sense, the agreement is excellent for  $^{198}\text{Pt}$  and acceptable for the other isotopes, depending on which error is used. A visible trend of the accuracy with mass cannot be established.

The temperature dependence of the ratios from Tab. VIII can, in principle, be used to study how well the energy dependence of the cross section is reproduced. The latter, in turn, is mainly determined by the low-energy tail of the GDR. In addition, there is a weaker dependence on the neutron potential in the exit channel. The effect of possible inaccuracies in the theoretical description of those properties are weakened, however, by the smoothing due to the integration over the effective Gamow-like energy window in the derivation of the rate. A direct comparison of cross sections may be more sensitive but the relevant quantity for astrophysics is the reaction rate.

As discussed before (Sec. IV B), the values derived by the use of the conventional method agree well with those of the superposition method, indicating that the threshold behavior of the  $(\gamma, n)$  cross section is roughly reproduced by Eq. (3.2). This is supported by the comparison to the  $(\gamma, n)$  cross sections of Ref. [25]. However, it cannot be expected in general that the cross section exhibits a structureless behavior proportional to  $\sqrt{E - E_{\text{thr}}}$ . The astrophysically relevant cross section depends on the dipole strength distribution in a narrow region above the threshold. Therefore, it is of importance to study this strength distribution experimentally. It is well known that the E1 strength exhibits significant fine structure like the so-called ‘pygmy resonance’ close to the particle threshold [16, 35–37]. The presence or absence of such a strength accumulation can change the astrophysical reaction rates significantly, while it will affect the position and width of the Gamow-like window on a small scale only.

There seem to be minor deviations between the two methods at  $T_9 = 2.0$  for  $^{198}\text{Pt}$  and at  $T_9 = 3.0$  for  $^{192}\text{Pt}$ . These minor discrepancies can be explained by the fact that the assumed threshold behavior of the cross section underestimates the cross section at higher energies (see also Fig. 8) which leads to a somewhat smaller slope of the reaction rate in the conventional analysis.

Within the errors the temperature dependence of the theoretical rates agrees with the data. Oddly enough, there seems to be a slight difference for  $^{198}\text{Pt}$  which is otherwise reproduced best. However, further conclusions can only be drawn pending a reduction of the experimental error bars.

Since the theoretical  $(\gamma, n)$  values have been confirmed for laboratory rates, detailed balance can be tested by comparing our stellar rates to the stellar photodisintegration rates derived from stellar neutron capture rates, as provided in Refs. [33, 38]. We find perfect agreement in all cases, confirming the validity of detailed balance.

As can be seen from Tab. VII, the stellar rates are larger by several orders of magnitude than the laboratory rates due to the facilitation of photodisintegration for thermally excited targets. This effect is sensitive to the used level density and structure but cannot be directly tested in the laboratory.

## VI. SUMMARY AND CONCLUSIONS

It has been shown that a thermal distribution of photons at astrophysically relevant temperatures can be simulated by the appropriate superposition of several bremsstrahlung spectra with different endpoint energies. Several platinum samples were irradiated with this quasi-thermal photon spectrum, and the  $(\gamma, n)$  reaction of  $^{190}\text{Pt}$ ,  $^{192}\text{Pt}$ , and  $^{198}\text{Pt}$  was analyzed using the photoactivation technique. The high sensitivity of this method allows the measurement of the  $(\gamma, n)$  reaction even for isotopes with very low natural abundances.

The measured reaction rates in the laboratory have been compared to a statistical model calculation, and good agreement was found for all analyzed isotopes. Furthermore, stellar reaction rates have been calculated which are enhanced by the thermal population of excited states in the target nucleus.

These photon induced reactions are important for the nucleosynthesis of the neutron-deficient p-nuclei which are synthesized in the astrophysical  $\gamma$  process in supernova explosions at temperatures of  $T_9 = 2 - 3$ . Almost no experimental data exist for the reactions relevant for the  $\gamma$  process. For a better understanding of the  $\gamma$  process more experimental data for  $(\gamma, n)$  and  $(\gamma, \alpha)$  reactions in the astrophysically relevant energy region are required. A systematic study is necessary to verify the predictions of statistical model calculations.

## ACKNOWLEDGMENTS

We thank the S-DALINAC group around H.-D. Gräf for the reliable beam during the photoactivation and U. Kneissl and A. Richter for valuable discussions. This work was supported by the Deutsche Forschungsgemeinschaft (contracts Zi 510/2-1 and FOR 272/2-1). T. R. is supported by a PROFIL professorship from the Swiss National Science Foundation (grants 2124-055832.98, 2000-061822.00) and by the NSF (grant NSF-AST-97-31569).

- 
- [1] D. L. Lambert, *Astron. Astrophys. Rev.* **3** (1992) 201.
- [2] M. Arnould and K. Takahashi, *Rep. Prog. Phys.* **62**, 395 (1999).
- [3] K. Langanke, *Nucl. Phys.* **A564** (1999) 330c.
- [4] G. Wallerstein *et al.*, *Rev. Mod. Phys.* **69** (1997) 995.
- [5] K. Ito, *Prog. Theor. Phys.* **26**, 990 (1961).
- [6] S. E. Woosley and W. M. Howard, *Astrophys. J. Suppl.* **36**, 285 (1978).
- [7] M. Rayet, N. Prantzos, and M. Arnould, *Astron. Astrophys.* **227**, 271 (1990).
- [8] M. Rayet, M. Arnould, M. Hashimoto, N. Prantzos, and K. Nomoto, *Astron. Astrophys.* **298**, 517 (1995).
- [9] N. Prantzos, M. Hashimoto, M. Rayet, and M. Arnould, *Astron. Astrophys.* **238**, 455 (1990).
- [10] W. M. Howard, B. S. Meyer, and S. E. Woosley, *Astrophys. J.* **373**, L5 (1991).
- [11] K. J. R. Rosman and P. D. P. Taylor, *Pure Appl. Chem.* **70**, 217 (1998).
- [12] P. Mohr, K. Vogt, M. Babilon, J. Enders, T. Hartmann, C. Hutter, T. Rauscher, S. Volz, A. Zilges, *Phys. Lett. B* **488**, 127 (2000).
- [13] A. Richter, *Proc. 5<sup>th</sup> European Particle Accelerator Conference*, Barcelona 1996, ed. S. Myers *et al.*, IOP Publishing, Bristol, 1996, p. 110.
- [14] P. Mohr, J. Enders, T. Hartmann, H. Kaiser, D. Schiesser, S. Schmitt, S. Volz, F. Wissel, and A. Zilges, *Nucl. Inst. Meth. Phys. Res. A* **423**, 480 (1999).
- [15] A. Zilges and P. Mohr, *Prog. Part. Nucl. Phys.* **44**, 39 (2000).
- [16] T. Hartmann, J. Enders, P. Mohr, K. Vogt, S. Volz, and A. Zilges, *Phys. Rev. Lett.* **85**, 274 (2000).
- [17] C. E. Rolfs and W. S. Rodney, *Cauldrons in the Cosmos*, The University of Chicago Press, Chicago 1988
- [18] P. Mohr, M. Babilon, J. Enders, T. Hartmann, C. Hutter, K. Vogt, S. Volz, and A. Zilges, *Proc. Nuclei in the Cosmos 2000*, ed. K. Langanke, in press.
- [19] J. Theuerkauf *et al.*, Program TV, Inst. f. Nuclear Physics, Universität zu Köln, unpublished.
- [20] P. Mohr, C. Hutter, K. Vogt, J. Enders, T. Hartmann, S. Volz, and A. Zilges, *Eur. Phys. J. A* **7**, 45 (2000)
- [21] R. Brun and F. Carminati, GEANT Detector Description and Simulation Tool, CERN Program Library Long Wwriteup W5013 edition, CERN, Geneva (1993).
- [22] V. Kölle *et al.*, *Nucl. Inst. Meth. Phys. Res. A* **431**, 160 (1999).
- [23] L. I. Schiff, *Phys. Rev. C* **83**, 252 (1951).
- [24] S. M. Seltzer and M. J. Berger, *Nucl. Instr. Methods* **B12** (1985) 95
- [25] A. M. Goryachev and G. N. Zalesnyĭ, *Sov. J. Nucl. Phys.* **27**, 779 (1978).
- [26] S. S. Dietrich and B. L. Berman, *At. Data Nucl. Data Tables* **38**, 199 (1988).
- [27] I. N. Boboshin, A. V. Varlamov, V. V. Varlamov, D. S. Rudenko, and M. E. Stepanov, The Centre for Photonuclear Experiments Data (CDFE) nuclear data bases, <http://depni.npi.msu.ru/cdfe>. INP Preprint 99-26/584, Moscow, 1999.
- [28] G. Audi and A. H. Wapstra, *Nucl. Phys.* **A595**, 409 (1995).
- [29] ENSDF data base, revision of 19-Aug-1999, using NNDC Online Data Service.
- [30] F. Ajzenberg-Selove, *Nucl. Phys.* **A506** (1990) 1.
- [31] W. A. Fowler, G. E. Caughlan, and B. A. Zimmerman, *Ann. Rev. Astron. Astrophys.* **5**, 525 (1967).
- [32] J. Holmes, S. Woosley, W. Fowler, and B. Zimmerman, *At. Data Nucl. Data Tables* **18**, 305 (1976).
- [33] T. Rauscher and F.-K. Thielemann, *At. Data Nucl. Data Tables* **75**, 1 (2000).
- [34] T. Rauscher, F.-K. Thielemann, and H. Oberhummer, *Ap. J. Lett.* **451**, L34 (1995).
- [35] J. Kopecky and M. Uhl, *Phys. Rev. C* **41** (1990) 941.
- [36] M. Igashira, H. Kitazawa, M. Shimizu, H. Komano, N. Yamamuro *et al.*, *Nucl. Phys.* **A457** (1986) 301.
- [37] J. Enders *et al.*, *Phys. Lett. B* **486**, 279 (2000).
- [38] Z. Y. Bao, H. Beer, F. Käppeler, F. Voss, K. Wisshak, and T. Rauscher, *At. Data Nucl. Data Tables* **76**, 1 (2000).

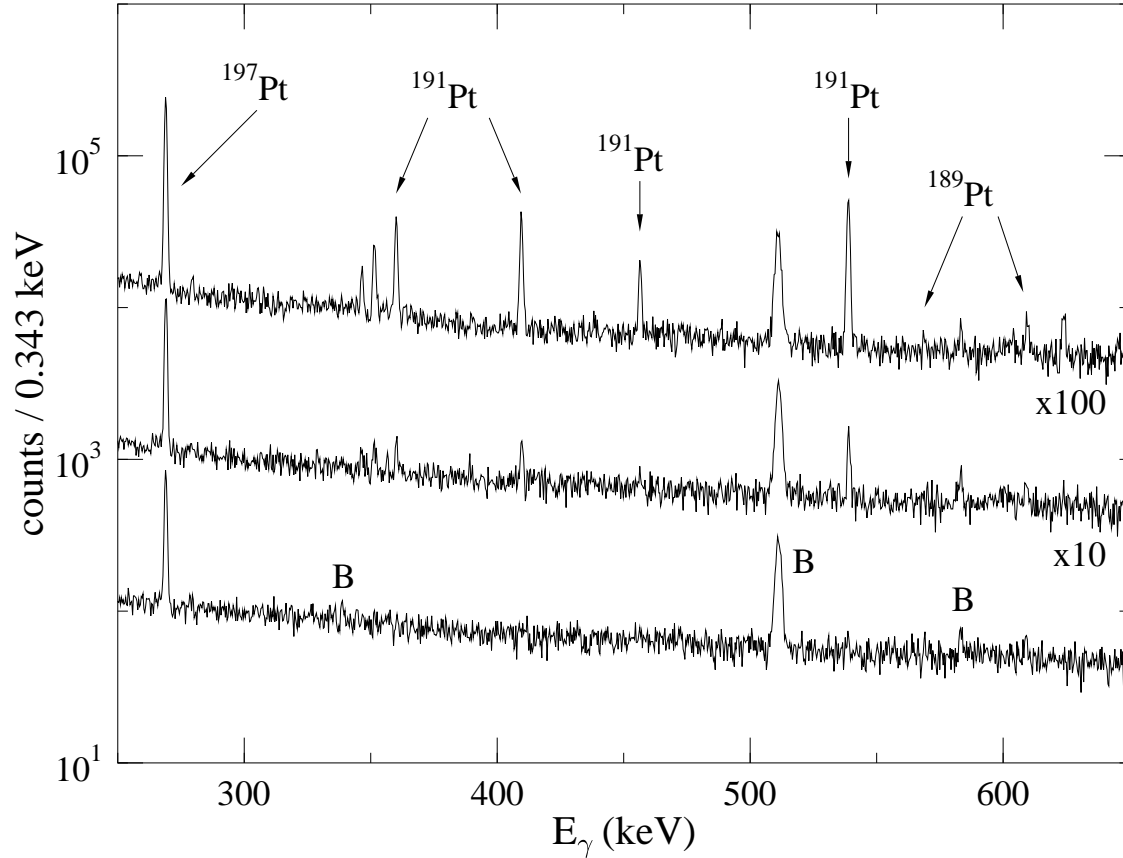


FIG. 1. Photon spectra of the activated platinum disks at the endpoint energies of  $E_0 = 9900$  ( $\times 100$ ),  $9450$  ( $\times 10$ ), and  $9000$  keV, from top to bottom. Shown is the energy region between 250 and 650 keV. For a full spectrum with all relevant lines, see [12]. The main peaks from the decay of  $^{189}\text{Pt}$ ,  $^{191}\text{Pt}$ , and  $^{197}\text{Pt}$  are indicated by arrows. Additional peaks from the background are labelled with B. The decay lines of  $^{189}\text{Pt}$  from the  $^{190}\text{Pt}(\gamma, n)^{189}\text{Pt}$  reaction are close to the sensitivity limit of this experiment because of the low 0.014% natural abundance of  $^{190}\text{Pt}$ . The lines of  $^{191}\text{Pt}$  from the  $^{192}\text{Pt}(\gamma, n)^{191}\text{Pt}$  reaction can hardly be seen in the lowest spectrum because the endpoint energy of  $E_0 = 9000$  keV is close to the neutron separation energy of 8676 keV (see Table I).



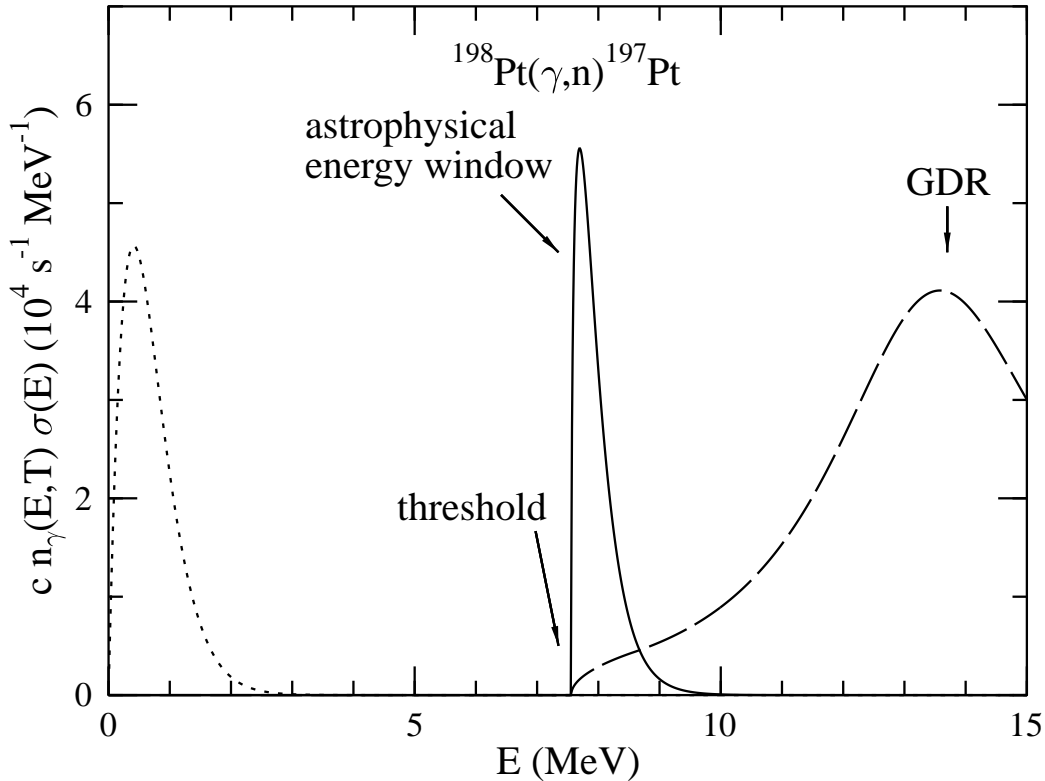


FIG. 2. Relevant energy window for  $(\gamma, n)$  reactions in a thermal photon bath with the temperature  $T_9 = 3.0$ . The integrand of Eq. (1.1) is given by the thermal Planck distribution  $n_\gamma(E, T)$  (dotted line) times the  $(\gamma, n)$  cross section  $\sigma(E)$  (dashed line). Note that the maximum of the integrand is located about  $kt/2$  above the threshold energy of  $E_{\text{thr}} = 7557 \text{ keV}$ , which was taken for the  $^{198}\text{Pt}(\gamma, n)^{197}\text{Pt}$  reaction from [28]. The GDR parameters were taken from experimental data by Goryachev *et al.* [25], and the threshold behavior  $\sigma \sim \sqrt{E - E_{\text{thr}}}$  was matched to the Lorentzian shaped cross section of the GDR 1 MeV above the threshold. Note that the assumption of a typical threshold behavior is not necessary for the determination of the quasi-thermal decay rate  $\lambda_{\text{qt}}$  (see text).

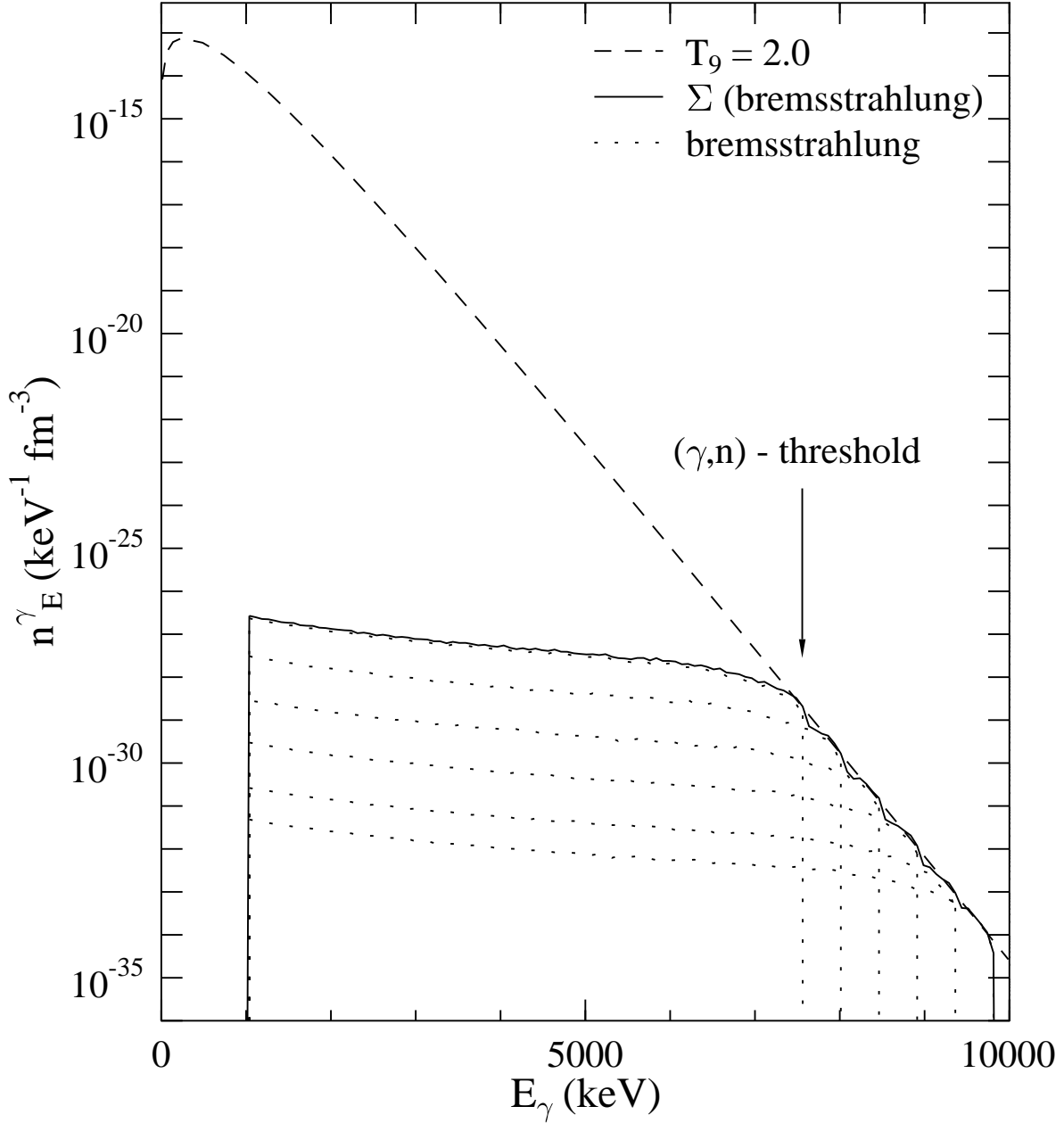


FIG. 3. The superposition of several bremsstrahlung spectra (full line) with different endpoint energies  $E_0$  is compared to the thermal Planck spectrum  $n_\gamma(E, T)$  (dashed line) at the temperature of  $T_9 = 2.0$ . Good agreement is found from 7.5 to 10 MeV with the superposition of only six endpoint energies. The six contributing bremsstrahlung spectra  $N_\gamma^{\text{brems}}(E_{0,i}, E)$  are shown as dotted lines. The arrow indicates the lowest  $(\gamma, n)$  threshold in our experiment from the  $^{198}\text{Pt}(\gamma, n)^{197}\text{Pt}$  reaction ( $E_{\text{thr}} = 7557$  keV). A figure which shows the superposition for a temperature of  $T_9 = 2.5$  can be found in [12].

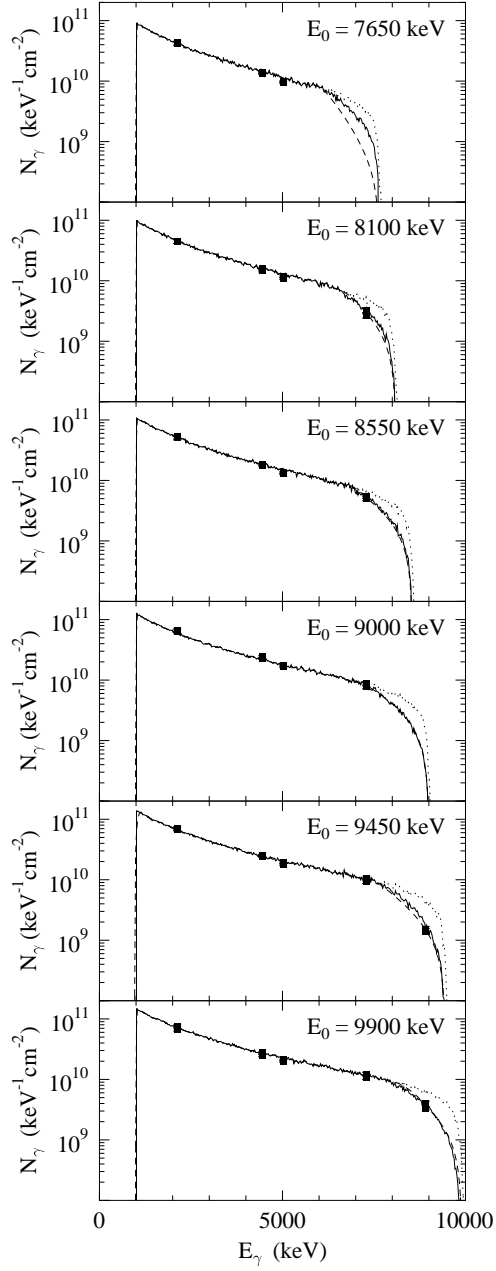


FIG. 4. Photon flux spectra calculated using the computer code GEANT (dotted line) at different endpoint energies  $E_0$ . In the high energy region, the GEANT spectra have been adjusted by the correction factor  $F$  in Eq. (3.7) (full line). The dashed lines show the results of the cubic spline interpolation. The squares represent the data points from the  $^{11}\text{B}(\gamma, \gamma')$  measurement.

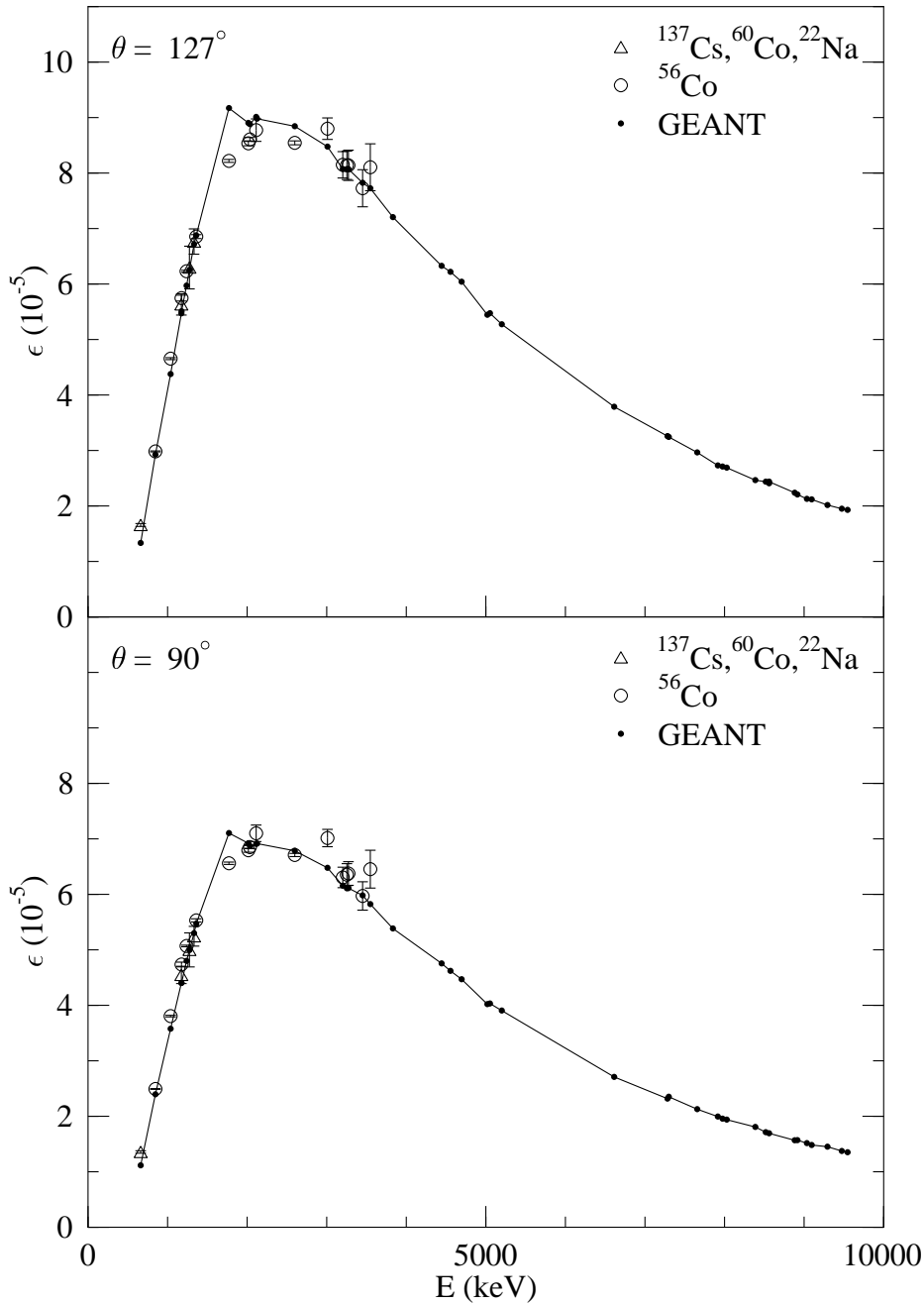


FIG. 5. Absolute efficiencies of the two detectors used for the  $^{11}\text{B}(\gamma, \gamma')$  measurements. The detectors were placed at  $\theta = 90^\circ$  and  $127^\circ$  relative to the incoming photon beam at distances of about 25 cm. The efficiencies have been determined using several calibration sources and are compared to a GEANT simulation. The data points from the GEANT simulation are connected by a line to guide the eye. The decrease at low energies comes from lead and copper filters in front of the detectors to reduce the background at low energies.

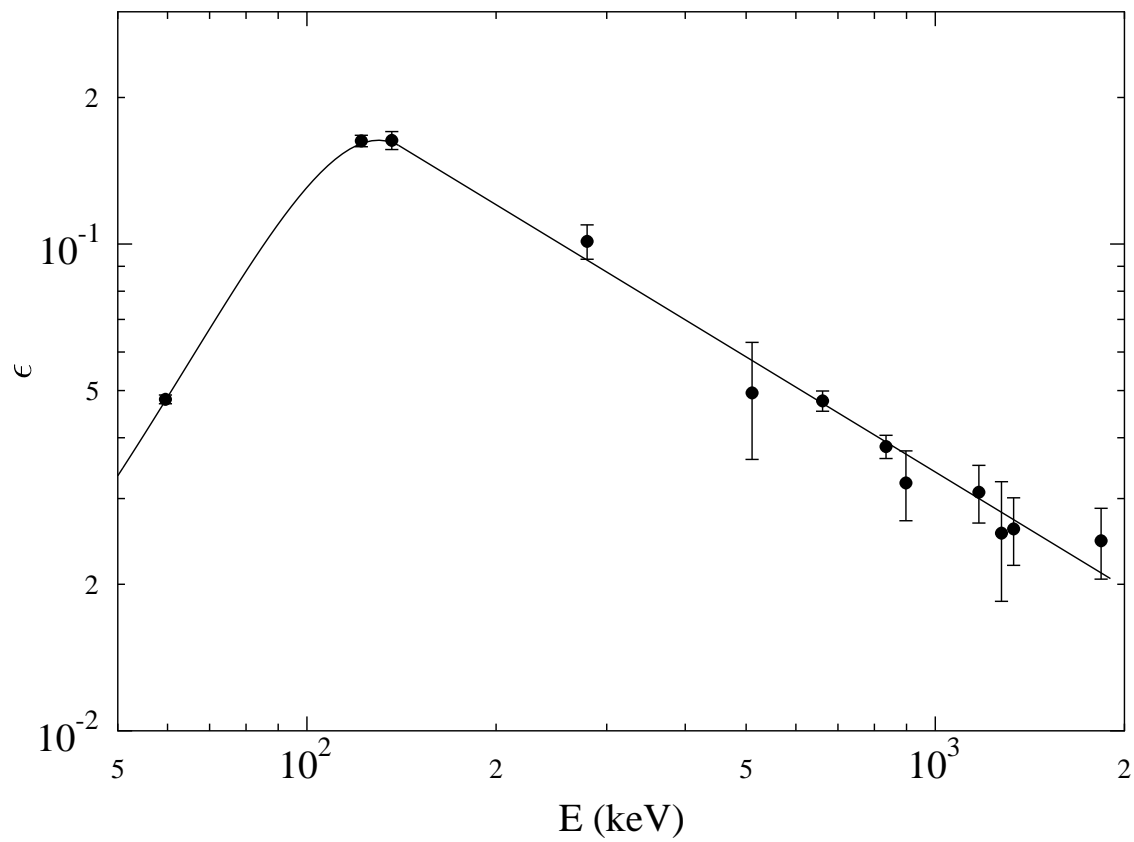


FIG. 6. Absolute efficiency of the 30 % HPGe detector: The data points are from the measurements with the calibration sources, the drawn line is an interpolation, which has been fitted to the data points with a least squares fit. Note the doubly logarithmic scale.

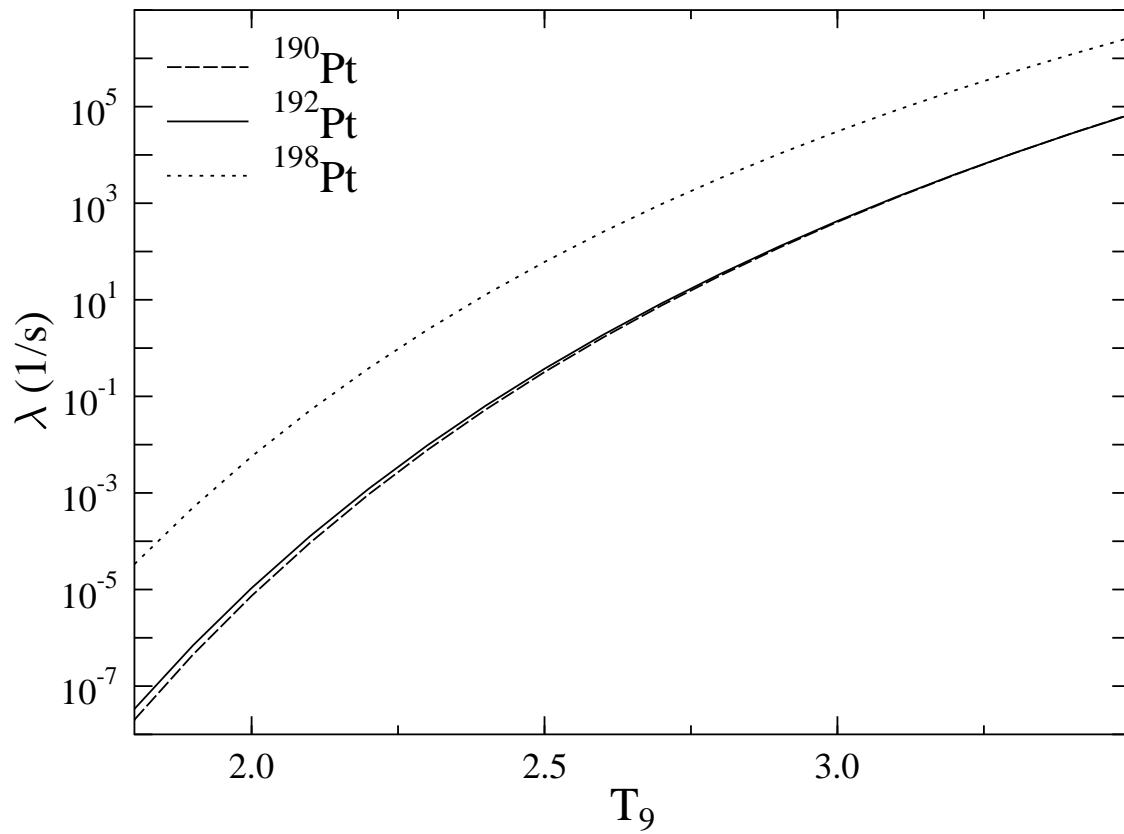


FIG. 7. Temperature dependence of the  $(\gamma, n)$  reaction rates  $\lambda$  in the complete relevant temperature region from  $T_9 = 2 - 3$ . The values have been calculated by the superposition of the different bremsstrahlung spectra.  $T_9$  is the temperature in  $10^9$  K. Note the much larger reaction rate of  $^{198}\text{Pt}$  because of the significantly smaller neutron separation energy.

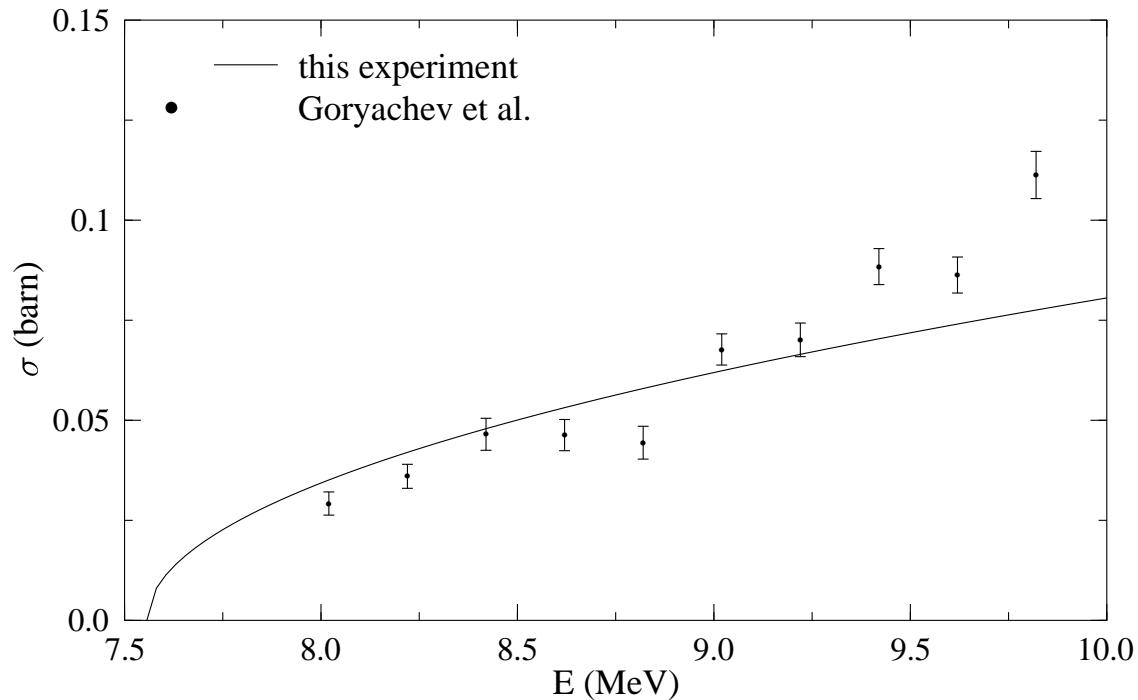


FIG. 8. Comparison of our results for the  $(\gamma, n)$  cross section of  $^{198}\text{Pt}$  to a previous experiment by Goryachev *et al.* [25].

TABLE I. Properties of the examined platinum isotopes and the decay  $\gamma$  rays following the electron capture or  $\beta^-$  decays. The absolute intensities have been taken from [29]. Note the big errors in the absolute intensities, resulting from a large uncertainty in the conversion factor from relative to absolute intensities in [29].

reaction	$E_{\text{thr}}$ (keV)	daughter	decay	energy (keV)	intensity per decay
$^{190}\text{Pt}(\gamma, n)^{189}\text{Pt}$	8911	$^{189}\text{Ir}$	$\epsilon$	568.9	$0.071 \pm 0.006$
				608.0	$0.081 \pm 0.021$
$^{192}\text{Pt}(\gamma, n)^{191}\text{Pt}$	8676	$^{191}\text{Ir}$	$\epsilon$	360.0	$0.06 \pm 0.015$
				409.4	$0.08 \pm 0.021$
				538.9	$0.137 \pm 0.035$
$^{198}\text{Pt}(\gamma, n)^{197}\text{Pt}$	7557	$^{197}\text{Au}$	$\beta^-$	77.4	$0.172 \pm 0.025$
				191.4	$0.037 \pm 0.004$
				268.8	$0.0023 \pm 0.0003$

TABLE II. Results for the cross section parameter  $\sigma_0$ . The values are weighted averages over all measured lines of the respective isotope. The values in the last column are weighted averages of the first two, except for  $^{190}\text{Pt}$ , where the result of an additional measurement has been included (details see Sec. IV A).

isotope	$\sigma_0$ (mb) interpolation	$\sigma_0$ (mb) correction factor	$\sigma_0$ (mb) average
$^{190}\text{Pt}$	$488 \pm 146$	$518 \pm 153$	$300 \pm 100^{\text{a}}$
$^{192}\text{Pt}$	$118 \pm 34$	$103 \pm 30$	$111 \pm 32$
$^{198}\text{Pt}$	$161 \pm 27$	$142 \pm 24$	$152 \pm 25$

<sup>a</sup>including additional measurement (see Sec. IV A).

TABLE III. Properties of the  $^{11}\text{B}$  levels which were used for the determination of the shape of the bremsstrahlung spectra by the  $^{11}\text{B}(\gamma, \gamma')$  measurement. The decay widths  $\Gamma$  were taken from the compilation [30].  $I$  is the energy-integrated cross section.

$E_x$ (keV)	$\Gamma_0/\Gamma$	$\Gamma$ (eV)	$I$ ( $10^3 \text{ eVfm}^2$ )
2124.7	1	0.12	$5.1 \pm 0.4$
4443.9	1	0.56	$16.3 \pm 0.5$
5019.1	0.856	1.963	$21.9 \pm 0.8$
7282.9	0.87	1.149	$9.5 \pm 0.7$
8916.3	0.95	4.368	$28.6 \pm 1.4$



TABLE IV. Average weighted values of the  $(\gamma, n)$  reaction rate  $\lambda$  for the nucleus  $^{192}\text{Pt}$  in the complete temperature range relevant for the astrophysical  $\gamma$  process.

temperature ( $10^9$ K)	$\lambda$ conventional <sup>a,b</sup> ( $\text{s}^{-1}$ )	$\lambda$ superposition <sup>a</sup> ( $\text{s}^{-1}$ )
2.0	$(9.6 \pm 0.7) \times 10^{-6}$	$(10.7 \pm 2.7) \times 10^{-6}$
2.1	$(1.14 \pm 0.09) \times 10^{-4}$	$(1.28 \pm 0.29) \times 10^{-4}$
2.2	$(1.09 \pm 0.08) \times 10^{-3}$	$(1.22 \pm 0.25) \times 2.10^{-3}$
2.3	$(8.50 \pm 0.63) \times 10^{-3}$	$(9.67 \pm 1.83) \times 10^{-3}$
2.4	$(5.62 \pm 0.42) \times 10^{-2}$	$(6.46 \pm 1.13) \times 10^{-2}$
2.5	$0.320 \pm 0.024$	$0.372 \pm 0.060$
2.6	$1.60 \pm 0.12$	$1.88 \pm 0.29$
2.7	$7.11 \pm 0.53$	$8.47 \pm 1.22$
2.8	$28.4 \pm 2.1$	$34.3 \pm 4.7$
2.9	$104 \pm 8$	$126 \pm 17$
3.0	$346 \pm 26$	$428 \pm 55$

<sup>a</sup> the calculated values of  $\lambda$  are subject to an additional error of 27.8% resulting from the uncertainty in the absolute intensity of the respective  $^{191}\text{Pt}$  lines and the uncertainty in the efficiency of the detectors used for the  $(\gamma, \gamma')$  measurement.

<sup>b</sup> an additional error resulting from the approximation of the shape of the cross section taken from Eq. (3.2) cannot be estimated.

TABLE V. Average weighted values of the  $(\gamma, n)$  reaction rate  $\lambda$  for the nucleus  $^{198}\text{Pt}$  in the complete temperature range relevant for the astrophysical  $\gamma$  process.

temperature ( $10^9$ K)	$\lambda$ conventional <sup>a,b</sup> ( $\text{s}^{-1}$ )	$\lambda$ superposition <sup>a</sup> ( $\text{s}^{-1}$ )
2.0	$(7.19 \pm 0.25) \times 10^{-3}$	$(5.68 \pm 1.00) \times 10^{-3}$
2.1	$(6.26 \pm 0.22) \times 10^{-2}$	$(5.14 \pm 0.84) \times 10^{-2}$
2.2	$0.449 \pm 0.016$	$0.383 \pm 0.057$
2.3	$2.73 \pm 0.10$	$2.39 \pm 0.33$
2.4	$14.3 \pm 0.5$	$12.9 \pm 1.7$
2.5	$65.6 \pm 2.3$	$60.8 \pm 7.3$
2.6	$269 \pm 10$	$255 \pm 29$
2.7	$996 \pm 35$	$961 \pm 102$
2.8	$(3.37 \pm 0.12) \times 10^3$	$(3.31 \pm 0.33) \times 10^3$
2.9	$(1.05 \pm 0.04) \times 10^4$	$(1.05 \pm 0.1) \times 10^4$
3.0	$(3.03 \pm 0.11) \times 10^4$	$(3.07 \pm 0.27) \times 10^4$

<sup>a</sup> the calculated values of  $\lambda$  are subject to an additional error of 16.3% resulting from the uncertainty in the absolute intensity of the respective  $^{197}\text{Pt}$  lines and the uncertainty in the efficiency of the detectors used for the  $(\gamma, \gamma')$  measurement.

<sup>b</sup> an additional error resulting from the approximation of the shape of the cross section taken from Eq. (3.2) cannot be estimated.

TABLE VI. Average weighted values of the  $(\gamma, n)$  reaction rate  $\lambda$  for the nucleus  $^{190}\text{Pt}$  in the complete temperature range relevant for the astrophysical  $\gamma$  process. Calculated using the conventional method.

temperature ( $10^9$ K)	$\lambda^{\text{a,b}}$ ( $\text{s}^{-1}$ )
2.0	$7.38 \times 10^{-6}$
2.1	$9.32 \times 10^{-5}$
2.2	$9.37 \times 10^{-4}$
2.3	$7.73 \times 10^{-3}$
2.4	$5.36 \times 10^{-2}$
2.5	0.319
2.6	1.66
2.7	7.65
2.8	31.7
2.9	119
3.0	409

<sup>a</sup>the calculated values of  $\lambda$  are subject to an error of 33%.

<sup>b</sup>an additional error resulting from the approximation of the shape of the cross section taken from Eq. (3.2) cannot be estimated.

TABLE VII. Theoretical  $(\gamma, n)$  reaction rates in 1/s for the target in the ground state  $\lambda^{\text{gs}}$  and a thermally excited target  $\lambda^*$ , calculated with the NON-SMOKER code.

Temperature $10^9$ K	$^{190}\text{Pt}$		$^{192}\text{Pt}$		$^{198}\text{Pt}$	
	$\lambda^{\text{gs}}$	$\lambda^*$	$\lambda^{\text{gs}}$	$\lambda^*$	$\lambda^{\text{gs}}$	$\lambda^*$
2.0	$4.11 \times 10^{-6}$	$1.70 \times 10^{-2}$	$1.75 \times 10^{-5}$	$4.58 \times 10^{-2}$	$6.85 \times 10^{-3}$	$1.66 \times 10^0$
2.5	$1.80 \times 10^{-1}$	$7.47 \times 10^2$	$5.71 \times 10^{-1}$	$1.41 \times 10^3$	$5.79 \times 10^1$	$1.49 \times 10^4$
3.0	$2.37 \times 10^2$	$9.23 \times 10^5$	$6.16 \times 10^2$	$1.35 \times 10^6$	$2.52 \times 10^4$	$6.32 \times 10^6$

TABLE VIII. Ranges of the ratio  $\lambda^{\text{gs}}/\lambda^{\text{exp}}$  determined by the quoted errors on the experimental rates. Except for  $^{190}\text{Pt}$ , the values extracted by the superposition method are used.

Temperature $10^9$ K	$^{190}\text{Pt}$	$^{192}\text{Pt}$	$^{198}\text{Pt}$
	$\lambda^{\text{gs}}/\lambda^{\text{exp}}$	$\lambda^{\text{gs}}/\lambda^{\text{exp}}$	$\lambda^{\text{gs}}/\lambda^{\text{exp}}$
2.0	0.42 – 0.83	1.31 – 2.19	1.03 – 1.46
2.5	0.42 – 0.84	1.32 – 1.83	0.85 – 1.08
3.0	0.44 – 0.87	1.28 – 1.65	0.75 – 0.90